Mechanical Systems and Signal Processing 202 (2023) 110689

Contents lists available at ScienceDirect

Mechanical Systems and Signal Processing

journal homepage: www.elsevier.com/locate/ymssp

Centrifugal forces enable band gaps that self-adapt to synchronous vibrations in rotating elastic metamaterial

Ignacio Arretche *, Kathryn H. Matlack

Department of Mechanical Science and Engineering, University of Illinois Urbana-Champaign, 1206 W Green St., Urbana, IL 61801, United States

ARTICLE INFO

Keywords:
Torsional vibrations
Tunable metamaterials
Rotor dynamics
Synchronous vibrations
Band gaps

ABSTRACT

The rotation of mechanical systems can greatly change their modal and wave propagation response. In the classic example of the Foucault pendulum, the Coriolis force from the Earth's rotation causes the pendulum path to appear deflected to an observer on Earth. More recently, Coriolis forces and gyroscopic effects from rotation have been shown to break time-reversal symmetry, induce non-reciprocity, and change the band structure of phononic crystals. However, rotation also introduces centrifugal forces that can considerably affect the vibration response through stress stiffening and spin softening effects. Although this is well studied in the field of rotor dynamics, the effects of centrifugal forces on the dynamic behavior of acoustic metamaterials (AMs) are still unexplored. In this paper, we study the dependence of torsional band gaps on rotational speed in a rotating shaft with attached local resonances. Different from previous studies, we explicitly consider the effects of stress stiffening in local resonances by introducing a stress stiffening function in a reduced order model of the rotating AM. We then calculate the stress stiffening function for beam-tip-mass resonators and show that these resonators have a resonant frequency that scales linearly with the rotational speed in the asymptotic limit, which in turn causes the band gaps of the AM to depend linearly on the rotational speed. Motivated by the presence of synchronous vibrations in rotating machinery, in which frequency is also linearly dependent on rotational speed, we show that this rotating AM supports band gaps that self-adjust to the synchronous vibration frequency, resulting in attenuation over a wide range of frequencies and thus rotational speeds. Finally, we validate the reduced order model of the rotating AM using 3D finite element analysis. This work contributes a foundational understanding of the effects of rotation in AMs and builds a connection between the AM and rotor dynamics communities, with the potential to introduce novel vibration control in rotor dynamics problems.

1. Introduction

Phononic crystals (PCs) and acoustic metamaterials (AMs) can control waves in unprecedented ways [1]. The addition of rotation in PCs and AMs has been shown in a limited capacity to broaden the scope of novel wave propagation phenomena. Coriolis forces in a rotating lattice can break time-reversal symmetry to achieve one-way topologically protected edge modes [2] and generate non-reciprocity in elastic [3] waves. One-way elastic waves can also be realized by leveraging the gyroscopic effect through gyroscopes located at nodes of hexagonal lattices [4,5]. In addition, gyroscopic effects in rotating beams with periodic inserts [6] and with periodic

* Corresponding author.
E-mail addresses: ia6@illinois.edu (I. Arretche), kmatlack@illinois.edu (K.H. Matlack).

https://doi.org/10.1016/j.ymssp.2023.110689
Received 14 January 2023; Received in revised form 24 June 2023; Accepted 11 August 2023
Available online 20 August 2023

resonances [7] can affect the modal frequencies and induce changes in the band structure.

However, rotation also induces centrifugal forces that yield stress stiffening and spin softening effects [8]. Even though these effects have been thoroughly studied in other fields such as rotor dynamics [8–11], studies in rotating AMs and PCs generally neglect these effects [2,3,6,7] because they were negligible for the configurations considered or were irrelevant to the objectives of those studies. The effects of stress stiffening from centrifugal forces were studied in the underlying beam structure of a metamaterial [12], however, stress stiffening was not considered in the actual resonators in that model. In fact, the effects from stress stiffening due to rotation in local resonances in AMs have been neglected this far. Resonances in AMs are typically realized using beams with tip masses [13–15] or slender plates with center masses [16,17]. Since the stiffness of slender beams and plates is strongly affected by tensile forces [8,17–19], these types of resonances will be strongly affected by the stress stiffening effect if they are oriented perpendicular to the axis of rotation. In these cases, the stress stiffening effect should have a strong influence on the response of the local resonances and thus on the overall dynamic behavior of the AM; to date, these effects have not been considered.

AMs spatially attenuate vibrations over a range of frequencies referred to as a band gap [20]. The lower edge frequency of this locally resonant band gap is determined by the resonance frequency of its resonators [21] (Fig. 1(b)). Since centrifugal forces in a rotating AM can generate strong changes in the stiffness of rotating elements [8,17–19], we can leverage these forces to realize an AM with band gaps that depend on rotation, i.e. a tunable AM with centrifugal forces as the tuning stimuli. Tunability is advantageous for AMs since it can broaden their operation ranges, which are typically limited because of their narrow band gaps. This is why different stimuli such as magnetic fields [22], thermal fields [23,24], electric fields [25], electric circuits [17], and mechanical forces [26], have been studied to tune AMs and PCs. However, centrifugal forces remain unexplored as a means of tuning band gaps.

In this paper, we study the effects of centrifugal forces in a rotating AM, specifically in terms of torsional wave propagation. Although torsional waves have been studied in PCs and AMs in terms of plane [27–30] and radial [31,32] wave propagation, the effects of rotation have not been considered. We are particularly motivated by the presence of torsional *synchronous vibrations* in rotating machinery [33,34]. These vibrations are excited by components that have circumferential periodic elements around the rotating axis, such as the cylinders in internal combustion engines [35] and reciprocating compressors [34], the cams on a camshaft [36], or teeth on gears [33,34]. Synchronous vibrations are characterized by frequencies that are linearly proportional to the rotational speed [33,34]:

$$\omega_S = N\Omega \tag{1}$$

where ω_S is the synchronous excitation frequency, Ω is the rotational speed and N is the order of the synchronous excitation. The rotational speeds at which the synchronous excitations and the resonant modes of the system coincide are referred to as *critical speeds* (Fig. 1(a)). At critical speeds, a resonance is excited by the synchronous excitation resulting in large vibration amplitudes, which can severely increase noise and cause damage to the system [33,34]. The goals of the current work are (1) to model and study how the stress stiffening effects can affect the wave propagation on rotating AMs and (2) to leverage the stress stiffening effects to realize an AM that self-adapts its band gap with rotational speed to attenuate synchronous excitations (Fig. 1(c)). This has important applications in preventing synchronous vibrations from reaching critical components in rotating machinery over a broad range of rotational speeds since the AM band gap self-adapts to the rotational speed (Fig. 1(c)).

This paper elucidates the effects of centrifugal forces on the propagation of torsional waves through a rotating AM composed of a homogenous shaft with attached local resonators. We first review the effects of rotation on elastic wave propagation to motivate the models of the study. We then introduce a reduced order model that captures the effects of rotation in the AM. We show the effect of stress stiffening and spin softening on the local resonances can be approximated by an effective stiffness that depends on rotational speed. In particular, the stress stiffening effect can be modeled by a stress stiffening function, the form of which depends on how the resonances are physically realized and on the orientation of the centrifugal forces. Although this stress stiffening function can be applied to different kinds of resonators, here, we calculate the stress stiffening function for a beam-tip-mass resonance model and show

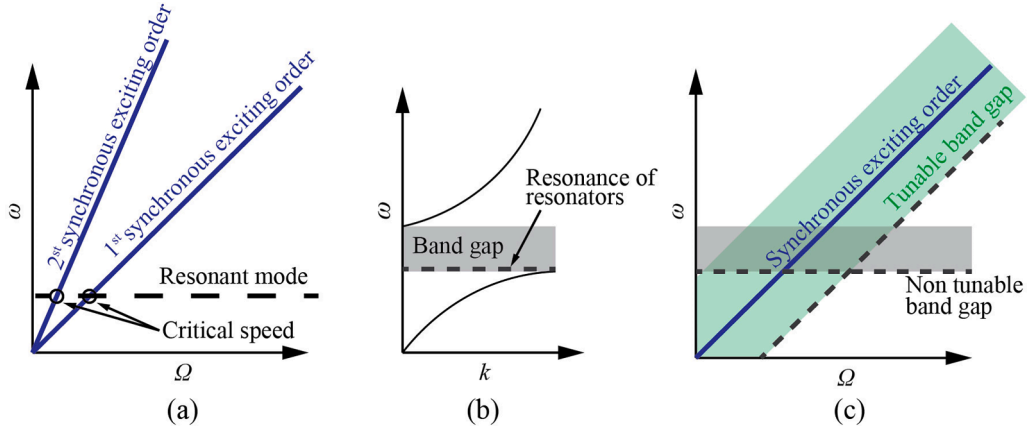

Fig. 1. (a) Schematic of synchronous orders and the interaction with resonant modes. (b) Typical band structure of locally resonant metamaterial. (c) Tunable band gaps and interaction with synchronous excitations.

that it is quadratic in the asymptotic limit. Analysis of the reduced order model shows that the rotating AM supports band gaps that are strongly dependent on rotational speed. By analyzing the dependence of the upper and lower edges of the band gap on rotational speed, we characterize the effects of rotation on the band gaps and the critical speeds of the system. This stress stiffening function results in band gaps that self-adjust to synchronous vibrations providing attenuation over broad frequency ranges. Finally, the finite element method is used to calculate the dispersion and transmission of a 3D rotating AM to validate the reduced order model.

2. Overview of effects of rotation in elastic wave propagation

Although we will restrain the problem to plane torsional waves through a shaft, it is helpful to review the effects of rotation on 3D wave propagation to identify the effects that need to be considered and how the system should be analyzed to include those effects. The most general 3D equations of motion that describe an elastic body rotating at a constant rotational speed in terms of a rotating frame of reference are [37,38],

$$\nabla \bullet \tilde{\sigma}(\vec{r},t) + \vec{F}_{ext}(\vec{r},t) = \rho \ddot{\vec{u}}(\vec{r},t) + \rho\vec{\Omega} \times \vec{\Omega} \times \vec{r} + \rho\vec{\Omega} \times \vec{\Omega} \times \vec{u}(\vec{r},t) + 2\rho\vec{\Omega} \times \dot{\vec{u}}(\vec{r},t) \tag{2}$$

where $\tilde{\sigma}$ is the stress tensor $\ddot{\vec{u}}$, $\dot{\vec{u}}$ and $\vec{u}$ are the acceleration, the velocity, and the displacement with respect to the rotating frame, respectively, $\vec{\Omega}$ is the rotational speed vector, $\vec{r}$ is the position vector in the rotating frame and $\vec{F}_{ext}$ are the external forces. Three main contributions arise from rotation: a time-independent centrifugal force $\left(\rho\vec{\Omega} \times \vec{\Omega} \times \vec{r}\right)$, a time-dependent centrifugal force $\left(\rho\vec{\Omega} \times \vec{\Omega} \times \vec{u}(\vec{r},t)\right)$, and a Coriolis force $\left(2\rho\vec{\Omega} \times \dot{\vec{u}}(\vec{r},t)\right)$.

The time-dependent part of the centrifugal force, commonly referred to as *spin softening*, and the Coriolis force are both dynamic forces. Spin softening arises from a change in centrifugal force due to the deformation of the solid and is a dynamic force that always points away from the equilibrium position [11], i.e. a destabilizing dynamic force. Coriolis forces couple the velocities that are in the plane perpendicular to the axis of rotation. Although they can be leveraged for time-reversal symmetry because of their proportionality to velocity [2], they can considerably complicate the analysis because they couple waves of different polarizations. The effects of Coriolis forces can have considerable effects [11,39], typically at high rotational speeds and careful attention must be given to be able to neglect these. Since they are dynamic forces, both Coriolis force and spin softening terms can be included in common analysis techniques for AMs, such as calculating the dispersion relation using the Bloch theorem.

The time-independent part of the centrifugal force is commonly referred to as *stress stiffening;* it has been thoroughly studied e.g. in rotor dynamics [8,11,40,41], but thus far ignored in AMs. Stress stiffening is a quasi-static force that shifts the equilibrium point of the vibration problem to a *prestressed* configuration, i.e. the vibrations will happen around a *prestressed* equilibrium point. The prestress can induce tensile and compressive forces that can considerably affect the bending stiffness of the system, particularly in thin plates [19] or beams [8,18]. Because stress stiffening arises from a quasi-static force (and not a dynamic force like spin softening and Coriolis effects), considering stress stiffening requires careful analysis, and if neglected it can lead to unrealistic solutions in certain configurations, as discussed in [9]. To include stress stiffening, a quasi-static problem must be solved first to find the new equilibrium stress state, and then the dynamics problem is solved by linearizing around this new stress state [8,11,40,41]. Note that this approach is only valid if the displacements around the new stress state are small enough that the stress stiffening can be approximated as constant during a vibration cycle, which we assume here; if this were not the case, nonlinear strain–displacement equations must be used [10,42].

Eq. (2) can also be solved numerically, and its discretized version can be calculated from the generalized Hamilton principle as [8,11],

$$M\ddot{u}(t) + G(\Omega)\dot{u}(t) + (K + K_G(u(t),\Omega) + K_S(\Omega))u(t) = F_C(\Omega) + F(t) \tag{3}$$

where M is the mass matrix, G is the Coriolis matrix, K, K_G and K_S are the stiffness, stress stiffening, and spin softening matrices, respectively, F_c is the vector of nodal centrifugal forces, F are the nodal external forces and u are the nodal displacements (refer to [11] for matrix definition). Taking the two-step approach previously described, we first solve a quasi-static problem, where we calculate the equilibrium position, u_0, and then pose a dynamic problem that is linearized around u_0,

$$(K + K_G(u_0,\Omega) + K_S(\Omega))u_0 = F_C(\Omega) \tag{4}$$

$$M\ddot{x}(t) + G(\Omega)(t) + (K + K_G(u_0,\Omega) + K_S(\Omega))u(t) = F(t) \tag{5}$$

Note that u in Eq. (5) now represents the displacement measured from u_0. To solve Eq. (4) and (5) numerically, we use COMSOL Multiphysics and run a two-step analysis. We first find the equilibrium position by using a nonlinear quasi-static analysis (Eq. (4)) and then run a linear dynamic analysis (either eigenfrequency or frequency sweep) linearized around the new equilibrium point (Eq. (5)).

3. Effects of rotation on a shaft with attached resonators

3.1. System description

Now that we have established the overall effects of rotation in wave propagation, we apply these concepts to plane torsional waves

propagating in an AM. We study an AM composed of a rotating shaft with attached lumped spring-mass local resonances (Fig. 2). The unit cell of the system is composed of a homogenous cylindrical shaft and a single degree of freedom resonator that couples with the angular displacements of the shaft (Fig. 2(c-e))). For simplicity, we depict a single resonator attached to the top of the shaft in the schematic (Fig. 2) but assume the geometry is axisymmetric. The infinite system is obtained by tessellating the unit cell (Fig. 2(c-e)) along the axis of the shaft (Fig. 2(a)). Under no rotation, the equations of motion that describe the propagation of plane axisymmetric torsional waves are,

$$\begin{cases} \rho J \dfrac{\partial^2 \theta(z,t)}{\partial t^2} = \mu J \dfrac{\partial^2 \theta(z,t)}{\partial x^2} + \sum_i \beta(\theta(z_i,t) - \theta_i(t))\delta(z - z_i) \\ I \dfrac{\partial^2 \theta_i(t)}{\partial^2 t} = \beta(\theta_i(t) - \theta(z_i,t)) \end{cases} \tag{6}$$

where μ, ρ, and J are the shear modulus, density, and polar moment of inertia of the shaft, respectively, θ is the angular displacement of the shaft, θ_i is the angular displacement of resonator i, z_i is the position of the resonator i, δ is the Kronecker delta function, and β and I are the equivalent torsional stiffness and mass moment of inertia of the resonators. We can calculate β and I from the resonator spring stiffness, k_y, and resonator mass, m as,

$$\beta = k_y R^2 \tag{7}$$

$$I = mR^2 \tag{8}$$

where R is the distance from the center of the axle to the mass of the resonator (Fig. 2(d)). We model the resonators in this way, and not a torsional spring and mass moment of inertia, because it eases the analysis of the effects of rotation (Section 3.2.1). The wave propagation through this infinitely periodic non-rotating system is well-known [21], and, given its periodic coefficients, is obtained using the Bloch theorem [43].

3.2. The effects of rotation on the dynamic response of the resonators

We seek an approximate set of equations that considers the effects of rotation on Eq. (6) to analytically understand how centrifugal forces influence the dynamics of the AM. Inspecting Eq. (6), we can separate the effects of rotation into two parts: (1) the effects of rotation on the plane torsional waves propagating through the shaft, i.e. $\theta(z,t)$ and (2) the effects of rotation on the resonators, i.e. $\theta_i(t)$. The selection of axisymmetric torsional waves is motivated by the fact that these modes are unaffected by rotation for small deformations (see [44] and Fig. S1), and thus rotation only affects the dynamic response of the resonators in this system. However, the concepts studied in this paper could be conducted on other wave polarizations that are affected by rotation, though the analysis would be more complex.

3.2.1. Effective stiffness captures the effects of rotation in 1DOF resonators

To isolate the effects of rotation on the resonators, we study a 1DOF reduced order resonator that rotates around an axis a distance R away from the mass (Fig. 3(a)). The dynamics of the rotating resonator around the prestressed equilibrium can be studied using Eq. (5). Neglecting Coriolis forces, the equation of motion of the rotating resonator is,

$$m\ddot{v} + \left(k_{0_y} + k_{G_y}(\Omega) - m\Omega^2\right)v = 0 \tag{9}$$

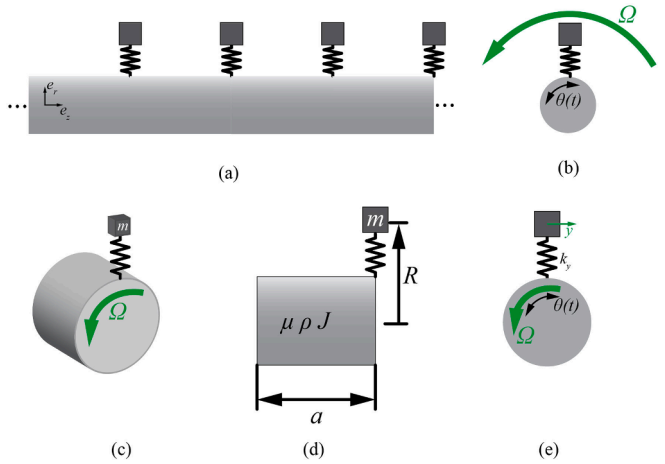

Fig. 2. Infinite AM: (a) side view, (b) front view. Unit cell (c) isometric view. (d) side view. (e) front view.

where v is the displacement in the y direction (Fig. 3(a)). The stiffness of the resonator is composed of 3 terms. The first term, k_{0_y}, represents the stiffness when there is no rotation. The second term models the stress stiffening effects and it distinguishes our study from previous rotating AM studies [12]. The stress stiffening term in Eq. (5) is modeled in Eq. (9) as an arbitrary *stress stiffening function*, $k_{G_y}(\Omega)$. Although in theory this stress stiffening function could take many forms, it will actually depend on how the resonances are realized (for example beam-tip-mass or plate-mass configurations) and how the centrifugal forces are imposed on the resonances as the AM rotates (i.e. the axis of rotation relative to the orientation, deformation, and DOF of the resonances). This will be studied in Section 3.2.2. Finally, the third part of the stiffness is the spin softening term, which is a negative stiffness with magnitude $m\Omega^2$. In summary, the effects of the centrifugal forces on the resonances can be captured by an effective stiffness, $k_{eff_y}(\Omega) = k_{0_y} + k_{G_y}(\Omega) - m\Omega^2$.

3.2.2. *The stress stiffening function of beam-tip-mass resonances*

Since the stress stiffening function depends on the physical realization of the resonances and the direction of the centrifugal force, we calculate the stress stiffening function of a beam-tip-mass resonator model, commonly used to realize resonances in AMs [13], to use in the reduced order model. This beam-tip-mass resonator will be later used in Sections 4 and 5 to demonstrate rotational effects in a rotating AM. The resonator consists of a cantilever beam of length L with a cubic mass at its tip of side s (Fig. 3(b)). The resonator rotates around an axle located at a distance r from its fixed boundary resulting in a centrifugal force that is parallel to the length of the beam. In contrast to previous numerical studies on the dynamics of rotating beams with tip masses [45,46], here we restrain the mass of the beam to be small compared to the tip mass because it allows us to obtain a closed-form solution of the stress stiffening function. This assumption results in (1) negligible centrifugal forces on the beam, thus, under rotation, the tension on the beam is constant and equal to the sum of centrifugal forces acting on the tip mass, (2) negligible beam dynamics such that the beam only contributes to the stiffness (and not the mass) of the reduced order model, and (3) negligible Coriolis forces on the beam. Under these conditions and considering that a vertical displacement of the tip mass causes bending deformation of the cantilever beam (Fig. 3(b)), the dynamics of the rotating beam-tip-mass resonators can be described by a reduced order mass-spring model (Fig. 3(a)), where the spring stiffness is equal to the quasi-static bending stiffness of a tensioned cantilevered beam and the mass is equal to the tip mass (Fig. 3(b)).

Rotation causes a tensile axial force, F_a, on the cantilever beam, where $F_a = m\Omega^2 R$, with m the mass of the tip, Ω the rotational speed, and R the distance from the center of rotation to the center of mass of the tip mass (Fig. 3(b)). Finding the deflection of the rotating beam is equivalent to finding the quasi-static deflection of a tensioned beam with tension F_a (Fig. 4(a)). The deflection of a tensioned cantilever beam is well known [47] (Eq. (S10)), and the bending stiffness of the beam can be calculated from deflection as,

$$k_b(F_n) = \frac{F_v}{v_b(L)} = \frac{\alpha F_a}{\alpha L - \tanh(\alpha L)} \tag{10}$$

where F_v is the magnitude of the vertical force at the tip of the beam, v_b is the vertical deflection, L is the length of the beam and $\alpha^2 = F_a/EI$, where E and I are Young's modulus and moment of inertia of the beam, respectively. Note that to capture the effects of the axial force on the stiffness (i.e. the stress stiffening effect) the solution cannot be simply computed from linear superposition but must be solved in the stressed (tensioned) configuration of the beam (see [47] or Supplemental Material for derivation). This is essentially a quasi-static equivalent to the two-step process described by Eqs. (4)-(5).

A good empirical approximation that accounts for discrepancies due to the finite geometry of the resonator is to use an effective length of the beam, $L_{eff} = L + s/2$ (see Supporting Material for details). The offset of the center of mass of the tip mass with respect to the tip of the beam (Fig. 3(b)) results in a lower effective bending stiffness of the beam. Further, the tip mass has a mass moment of inertia which may also affect the overall dynamics of the beam-tip-mass resonator [45]. Considering these effects prevents a closed-form solution (Eq. (10)) for the beam stiffness, however, the empirical approximation accurately approximates the resonator dynamic response when the dimensions of the resonator are within certain ranges (see Supporting Material for details).

Considering the bending stiffness of a non-rotating beam, $k_{0_y} = EI/L_{eff}^3$, the stress stiffening function of the beam-tip-mass resonator is,

$$k_{G_y}(\Omega) = k_b(\Omega) - \frac{EI}{L_{eff}^3} = \frac{\alpha m\Omega^2 R}{\alpha L_{eff} - \tanh(\alpha L_{eff})} - \frac{EI}{L_{eff}^3} \tag{11}$$

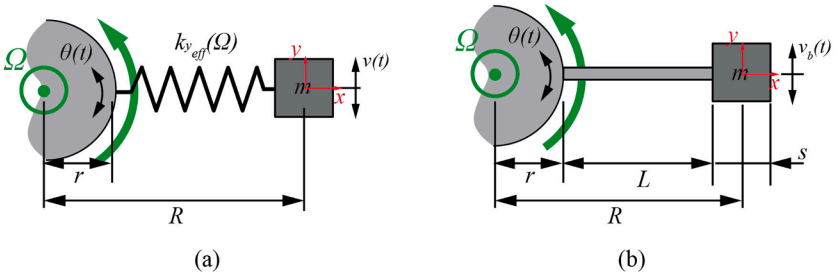

Fig. 3. (a) mass-spring resonator. (b) beam-tip-mass resonator.

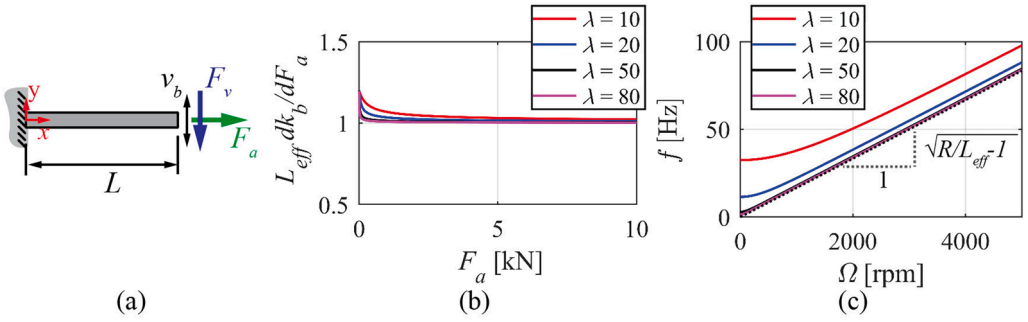

Fig. 4. (a) Quasi-static beam problem for calculation of stress stiffening function. (b) Normalized derivative of the stiffness with respect to the axial force. (c) Effect of rotation on the resonance frequency of resonators with different slenderness ratios and equal R/L_{eff}.

which results in the following effective stiffness of the resonator,

$$k_{y_{eff}}(\Omega) = \frac{\alpha m \Omega^2 R}{\alpha L_{eff} - \tanh(\alpha L_{eff})} - m\Omega^2 \tag{12}$$

The stiffness of the beam-tip-mass resonator strongly depends on the rotational speed and the stress stiffening function (Eq. (11)) can capture these effects as an effective spring stiffness in a reduced order model of the resonator (Eq. (9)).

Asymptotic analysis of the beam stiffness (Eq. (10)) as $\Omega \to \infty$ shows how the centrifugal forces affect the stiffness and thus the resonant frequencies for this type of resonator. Using a Taylor series expansion about an axial force F_{a0}, Eq. (10) can be approximated as,

$$k_b(F_a) = \frac{F_{a0}\alpha_o}{L_{eff}\alpha_0 - \tanh(\alpha_0 L_{eff})} + \frac{3L_{eff}F_{a0} - 3EI\tanh(\alpha_0 L_{eff}) - L_{eff}F_{a0}\tanh^2(\alpha_0 L_{eff})}{2EI\left(L_{eff}\alpha_0 - \tanh(\alpha_0 L_{eff})\right)^2}(F_a - F_{a0}) + O(F_a - F_{a0})^2 \tag{13}$$

where $\alpha_0 = \sqrt{F_{a0}/EI}$. Taking the limit as $F_{a0} \to \infty$,

$$k_b(F_a = m\Omega^2 R) \approx \frac{m\Omega^2 R}{L_{eff}} \tag{14}$$

At high values of rotation, the stiffening function is quadratic. This results in a linear asymptotic relationship between the resonance frequency of the resonator and rotational speed,

$$\omega_r(\Omega) = \sqrt{\frac{k_{y_{eff}}(\Omega)}{m}} \approx \sqrt{\left(\frac{R}{L_{eff}} - 1\right)}\Omega \tag{15}$$

Note $R/L_{eff} > 1$ for the asymptotic behavior of the resonance frequency to be linear and remain stable; i.e., the stress stiffening effect must overcome the spin softening effect to avoid dynamic instabilities at high speeds due to spin softening. Eq. (14) and (15) are asymptotic approximations, however, the beam has a non-zero static stiffness at zero rotational speed. In fact, the stress stiffening effect at low speeds takes a different relationship and can be calculated by setting $F_{a0} = 0$ in the Taylor series expansion (Eq. (13)),

$$k_b(F_a = m\Omega^2 R) = \frac{3EI}{L_{eff}^3} + \frac{6m\Omega^2 R}{5L_{eff}} + O(F_a^2) \tag{16}$$

The first term of Eq. (16) is the stiffness of the non-rotating beam, $3EI/L_{eff}^3$. Eqs. (14) and (16) show that the stress stiffening effect goes through a transition zone where the stress stiffening function asymptotically goes from $6m\Omega^2 R/5L_{eff}$ (Eq. (16)) to $m\Omega^2 R/L_{eff}$ (Eq. (14)). In the transition zone, the beam goes from a beam-like (reaction under bending) to a string-like (in-plane reaction) behavior. To further study when this transition occurs, we numerically calculate the derivative of Eq. (10) with respect to F_a (Fig. 4(b)) for different slenderness ratios, $\lambda = L_{eff}/t$. For small slenderness ratios, the beam-like behavior is stronger and thus, the transition zone extends to higher normal forces. In contrast, for high slenderness ratios, the beam approaches the string-like behavior at much lower forces. Here, the stress stiffening function is quadratic (Eq. (14)) and the relationship between the resonance frequency of the resonances and rotational speed is linear (Eq. (15) and Fig. 4(c)). As shown later in Sections 4 and 5, this asymptotically linear relation enables locally resonant band gaps to align with the frequency of synchronous excitations, since synchronous excitations also depend linearly on rotational speed.

3.2.3. *Effects of Coriolis forces on the resonances*

The equation of motion of the reduced order model (Eq. (9)) assumes Coriolis forces are neglected. To understand when this is the case for the specific beam-tip-mass resonator studied above, we consider that the resonator has two degrees of freedom (along x and y)

and stiffnesses along both DOFs (Fig. 5(a)). Coriolis forces couple the degrees of freedom that are perpendicular to the axis of rotation, thus the extra degree of freedom captures these effects. We don't include z-displacements in the analysis because these are parallel to the rotational speed vector and thus are uncoupled from x and y-displacements. For this 2DOF reduced order model to approximate the response of the beam-tip-mass model, the stiffness of the reduced order model in the x direction must be given by the axial stiffness of the beam. Under small deformation, the axial stiffness of the beam is not affected by the axial force, and thus there is no stress stiffening effect in the x-direction, i.e. $k_{Gx}(\Omega) = 0$. The dynamics of this 2DOF resonator around the prestressed (Eq. (5)) equilibrium are,

$$\begin{cases} m\ddot{u} - 2m\Omega\dot{v} + k_{eff\,x}(\Omega)u = 0 \\ m\ddot{v} + 2m\Omega\dot{u} + k_{y_{eff}}(\Omega)v = 0 \end{cases} \tag{17}$$

where $k_{eff\,x}(\Omega) = k_{0x} - m\Omega^2$, $k_{0x} = EA/L_{eff}$, and A is the cross-sectional area of the beam. The solution to this homogenous set of equations takes the form $\begin{Bmatrix} u \\ v \end{Bmatrix} = \begin{Bmatrix} U \\ V \end{Bmatrix} e^{\lambda t}$, where

$$\lambda^2 = -\frac{1}{2}\left(\frac{k_{eff\,x}(\Omega)}{m} + \frac{k_{eff\,y}(\Omega)}{m} + 4\Omega^2\right) \pm \frac{1}{2}\sqrt{\left(\frac{k_{eff\,x}(\Omega)}{m} + \frac{k_{eff\,y}(\Omega)}{m} + 4\Omega^2\right)^2 - \frac{4k_{eff\,x}k_{eff\,y}(\Omega)}{m^2}} \tag{18}$$

Fig. 5(b) shows the eigenfrequencies and normalized V when Coriolis forces are neglected vs. considered for different rotational speeds. When Coriolis effects are neglected (Fig. 5(b) – dashed lines), the y-polarized (bending) mode increases with rotation because of the stress stiffening effect (Eq. (10)). The x-polarized (axial) mode, on the contrary, softens due to spin softening. As expected, the two modes are completely decoupled. This is not the case when we consider Coriolis forces (Fig. 5(b) – solid lines). As the modal frequencies approximate each other, the modes repel, their polarizations are first mixed, and eventually swapped. This phenomenon is known as *mode veering* [48]. The Coriolis effect can only be neglected far away from the mode veering point. Note that Coriolis forces strongly affect the evolution of the mode, and the linear asymptotic behavior of Eq. (11) is lost close to the veering point. Further, near the veering point, the resonator modes have a mixed polarity (Fig. 5(b)) and thus, torsional and axial displacements in the shaft are coupled through the resonances, further complicating the problem. For this study, we limit the range of rotation to be far from the mode veering point such that we can neglect the Coriolis effects. We assume that Coriolis forces are negligible when the axial resonance frequency (ω_x) of the beam-tip-mass resonator is at least 5 times larger than ω_r. In this range, the torsional waves in the shaft will only excite the y-polarized (bending) mode of the resonator and the equation of motion can be reduced to a single degree of freedom (Eq. (9)).

4. Dynamics of the rotating AM: Self-adapting band gaps, critical speeds, and transmission

We now compile the analysis and approximations in Sections 3.1-3.2 to derive an approximate equation of motion of a rotating AM that considers the effects of centrifugal forces on local resonances. The wave propagation through the shaft is unaffected (see [44] and Supplemental Material) and thus, the parts of Eq. (6) that refer to the matrix wave propagation (i.e. $\partial^2\theta(z,t)/\partial t^2$ and $\partial^2\theta(z,t)/\partial x^2$) remain the same. The effects of the centrifugal forces on the resonators can be represented by an effective stiffness (Eq. (9)). The system analyzed can essentially be approximated as an AM that comprises a shaft with attached lumped resonances, whose stiffness depends on rotational speed,

$$\begin{cases} \rho J\dfrac{\partial^2\theta(z,t)}{\partial t^2} = \mu J\dfrac{\partial^2\theta(z,t)}{\partial x^2} + \displaystyle\sum_i k_{y_{eff}}(\Omega)R^2(\theta(z_i,t) - \theta_i(t))\delta(z - z_i) \\ mR^2\dfrac{\partial^2\theta_i(t)}{\partial^2 t} = k_{y_{eff}}(\Omega)R^2(\theta_i(t) - \theta(x_i,t)) \end{cases} \tag{19}$$

where $k_{y_{eff}}(\Omega)$ is given by Eq. (12). We refer to the model that describes the dynamic behavior of the rotating AM through Eq. (19) as the reduced order model of the rotating AM because the resonances are modeled as lumped masses and springs.We study the reduced order model to analytically elucidate key physics of the problem. Note that these equations of motion describe displacements around

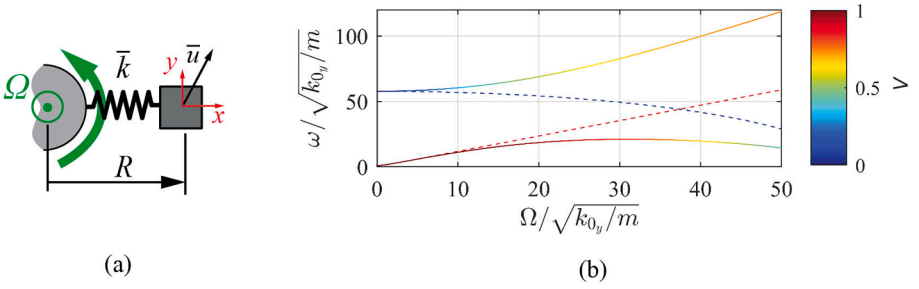

Fig. 5. (a) 2DOF resonator model. (b) Modal frequencies neglecting (dashed) considering (solid) Coriolis effects.

the prestressed equilibrium, and the effective stiffness of the resonators captures the stress stiffening effect. The dispersion relation of this system has a closed-form solution that depends on rotational speed [21],

$$k(\omega,\Omega)=\frac{1}{a}\cos^{-1}\left(\cos\left(\sqrt{\frac{\rho}{\mu}}\omega\right)-\frac{\omega k_{y_{eff}}(\Omega)R^2}{2J\sqrt{\mu\rho}\left(\omega_r^2(\Omega)-\omega^2\right)}\sin\left(\sqrt{\frac{\rho}{\mu}}\omega\right)\right) \tag{20}$$

This system has one locally resonant band gap and an infinite set of Bragg band gaps. Although we limit our study to the stress stiffening function of the beam-tip-mass resonator (Eq. (12)), this dispersion is valid for any stress stiffening function if Coriolis forces can be neglected. The stress stiffening function of beam-tip-mass resonators (Eq. (12)) creates a linear asymptotic dependence of resonance frequencies on rotation (Fig. 4(c)), meaning the band gap should linearly depend on the rotational speed. This enables band gaps to align with the frequency of synchronous excitations since synchronous excitations also depend linearly on rotational speed. Furthermore, different values of R/L_{eff} (Eq. (15)) reveal how this stress stiffening function can control the critical speeds of this system. This makes an AM that exhibits this stress stiffening function a rich fundamental study.

To further understand the relationship between band gaps and the synchronous excitation in the rotating AM, we calculate the dependence of the band gap edges on rotational speed. Using the asymptotic expression for ω_r (Eq. (15)) and considering the locally resonant band gap is much lower than the first Bragg band gap, we can approximate the lower, ω_{low}, and upper, ω_{high}, edges of the first locally resonant band gap as [21],

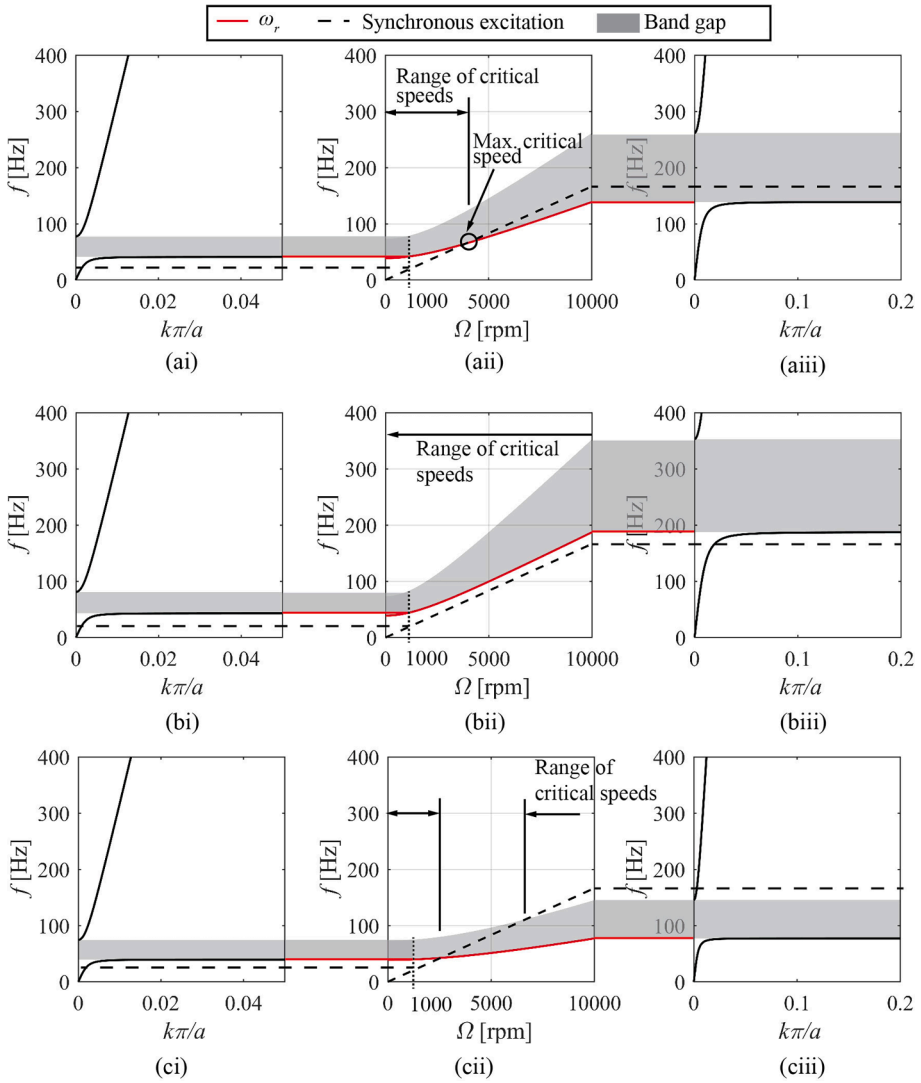

Fig. 6. Dependance of band structure on rotational speed for N = 1 and (a) 1/D < b < 1, (b) b > 1, and (c) b < 1/D. (i) Band structure at Ω = 1000rpm, (ii) band gaps vs. Ω, and (iii) band structure at Ω = 10000rpm. The band structures are not shown for the entire Brillouin zone for clarity. In the region of the Brillouin zone that is not shown, the first pass band remains approximately horizontal.

$$\omega_{low}(\Omega) \approx \omega_r(\Omega) \approx \sqrt{\left(\frac{R}{L_{eff}} - 1\right)}\Omega \tag{21}$$

$$\omega_{high}(\Omega) \approx D\omega_r(\Omega) \approx D\sqrt{\left(\frac{R}{L_{eff}} - 1\right)}\Omega \tag{22}$$

where $D = \sqrt{1 + \frac{mR^2}{\rho Ja}}$. Note that both the upper and lower edges of the band gap depend linearly on rotational speed Ω. Since $D > 0$, the upper edge increases with rotation at a higher rate than the lower edge (Fig. 6). The band gaps open as rotational speed increases, and thus they are present at all rotational speeds.

The critical speeds of the system do not exist when the synchronous vibration frequency falls in the band gap, since the AM has no resonant modes inside the band gap. Thus, the frequencies at which critical speeds exist depend on how the synchronous vibrations relate to the rate of change of the band gap edges with rotation (i.e. the slope of the upper and lower edges, Fig. 6). To characterize this relationship, we introduce a parameter b such that,

$$\sqrt{\frac{R}{L_{eff}} - 1} = b\mathrm{N} \tag{23}$$

The lower band gap edge is defined by bNΩ (Eq. (21)) and the upper band gap edge by DbNΩ (Eq. (22)). If $1/D < b < 1$ (Fig. 6(a)), the synchronous excitation increases with speed at a rate that is between the rates of the lower and upper band gap edges. Therefore, the synchronous excitation falls inside the band gap for all speeds above a certain rotational speed (Fig. 6(aii)). Since no modes exist

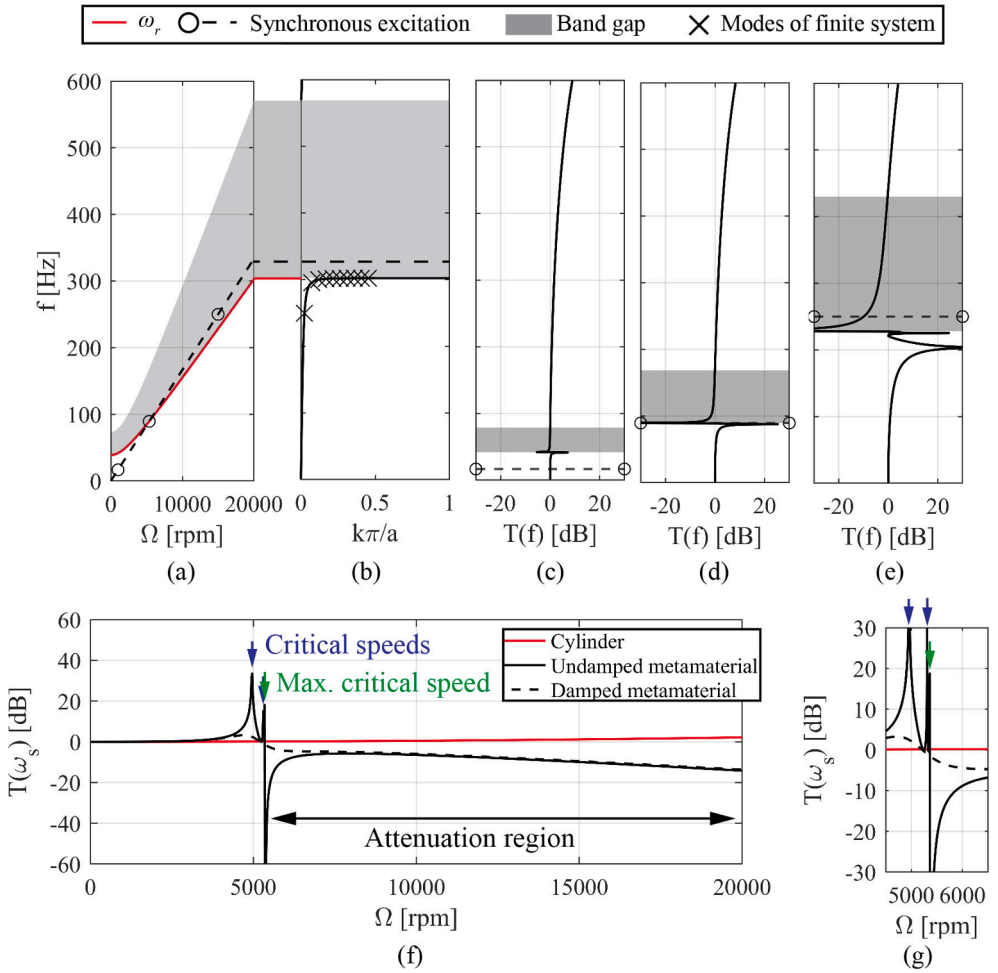

Fig. 7. (a) Band gaps for N = 1, b = 0.9, C = 1.9. (b) Band structure for Ω = 20000rpm. Transmission curves for (c) Ω = 1000 rpm, (d) Ω = 5365rpm (maximum critical speed), (e) Ω = 15000rpm. (f) Transmission at the synchronous excitation frequency. (g) Zoom-in of view of (f) around maximum critical speed.

inside the band gap, the synchronous excitation and a resonant mode of the system will not coincide above this rotational speed and thus there is a *maximum critical speed of the system*. Furthermore, the synchronous excitation will be considerably attenuated for all speeds above this maximum critical speed because of the presence of evanescent modes inside the band gap. Essentially, *the band gap self-adapts with rotational speed* resulting in attenuation over a large range of frequencies/ rotational speeds.

The infinitely periodic rotating AM has an infinite number of non-evanescent modes that span each one of its pass bands [49], thus, there is an infinite number of critical speeds. If $1/D < b < 1$, the critical speeds are bounded since synchronous excitation only falls inside a pass band below a maximum critical speed (Fig. 6(aii)). However, picking different values of b results in different distributions of the critical speeds with the frequency of the system. If $b \geq 1$, the synchronous excitation increases with speed at a lower rate than the lower edge of the band gap (Fig. 6(b)). Thus, the excitation is inside the first pass band for all rotational speeds and the critical speeds span the entire rotational speed range. On the other hand, if $b > 1/D$, the synchronous excitation first falls inside the first pass band (Fig. 6(ci)), then inside a band gap (Fig. 6(cii)) and finally enters the second pass band (Fig. 6(ciii)). In this case, there are no critical speeds within a certain rotation range (Fig. 6(bii)).

To further study the system, we analyze the finite version using a 1D linear finite element code programmed in Matlab. We solve Eq. (19) for a 10-unit cell system with a plane torsional harmonic excitation at one end of the finite structure. We calculate transmission as the output angular displacement over input angular displacements for different excitation frequencies and rotational speeds (Fig. 7(c-e)). We also calculate the resonance frequencies of the 10-unit cell system under fix-free boundary conditions (Fig. 7(b)). This is done for the case where $1/D < b < 1$ since this case allows for attenuation of the synchronous vibrations over wide frequency ranges. We select $N = 1$, $b = 0.9$, and $D = 1.9$.

Above the maximum critical speed, the synchronous excitation is considerably attenuated (Fig. 7(e)). This is expected since the synchronous excitation falls inside the band gap for all rotational speeds above the maximum critical speed (Fig. 6(aii)). Below the maximum critical speed (Fig. 7(c)), there is no attenuation of the synchronous excitation while at the maximum critical speed (Fig. 7 (d)), the synchronous excitations coincide with a resonance frequency of the system. Because there are no truncation resonances in this finite system [50], there are 10 resonances inside the first pass band of the 10-unit cell AM (Fig. 7(b)) and no resonances inside the band gap. For this reason, the finite system has a finite number of critical speeds that are bounded by the same maximum critical speed as the infinite system.

We further study the transmission at the synchronous excitation frequency, i.e. $T(\omega_s)$, as a function of rotational speed (Fig. 7(f)) to determine the number of critical speeds and attenuation regions of the finite system. The number of critical speeds depends on the number of unit cells, the synchronous excitation order, and the evolution of the band structure with rotation. The finite system will always have at least one critical speed and no more critical speeds than its number of unit cells. For the case studied here, there are 3 critical speeds (Fig. 7(f,g)). The critical speeds could be detrimental when e.g. increasing the rotational speed from 0 to a finite value. However, the stiffness of the resonators at the lower speeds is small because the stress stiffening effect is small. Thus, with some small amount of damping, for example, an isotropic loss factor of 0.05 (typical of hard polymers [51]) these resonances can be considerably attenuated (Fig. 7(g)) avoiding damage as the system passes through the critical speeds. Note that this isotropic loss factor has a negligible effect on the attenuation region (Fig. 7(f)).

5. Self-adapting band gaps in the 3D rotating AMs

In this section, we use 3D finite element simulations (Eqs. (4)-(5)) to show that a 3D physical model with the beam-tip-mass resonances shows similar self-aligning band gaps as the reduced order model in Section 4. The 3D model contains an array of the physical resonators presented in Section 3 distributed circumferentially (Fig. 9-insets) in each unit cell. A circumferential array (1) ensures that centrifugal moments are balanced as the system rotates, and (2) allows for a larger total mass of resonators compared to the mass of the shaft, thus widening the band gaps (Eq. (22)). In the axisymmetric torsional wave, all resonators move in phase and thus we can still compare the 3D case to the reduced order model, by modeling the array with a single degree of freedom and modifying Eqs. (7)-(8) such that,

$$\beta(\Omega) = nk_{y_{eff}}(\Omega)R^2 \tag{24}$$

$$I = nmR^2 \tag{25}$$

where n is the number of resonators in the circumferential array. In the 3D rotating AM, the shaft, the beams, and the cubic masses are modeled with 3D tetrahedral elements. We model a single unit cell (Fig. 9(ai, bi) – inset) and use Floquet boundary conditions to find the dispersion relation at different rotational speeds. We extract the lower and upper bounds of the axisymmetric plane torsional band gap (Fig. 9(ai, bi)). We also calculate numerical transmission at the synchronous frequencies, i.e. $T(\omega_s)$, by running a frequency sweep analysis on a 10-unit cell finite metamaterial (Fig. 9(aii, bii) – inset) for different rotational speeds (Fig. 9(aii, bii)). We design and numerically validate two AMs, one that attenuates first-order synchronous vibrations (Fig. 9(a)) and another that attenuates second-order synchronous vibrations (Fig. 9(b)), to show that stress stiffening can tune several orders of synchronous vibrations. We use Eqs. (15) and (23) to design the different beams. We select the radius of the main shaft and the unit cell size to be 20 mm. There is no loss in generality here since picking different shaft sizes will simply result in different beam dimensions (Eq. (23)). We also limit the rotational speed to be below 20,000 rpm because this is a typical range for rotating machinery such as high-performance internal combustion engines [52,53], high-pressure compressors of turbines [54], and transonic compressors [55]. Table 1 shows the dimensions of the two AMs. To design the beam-tip-mass resonators, we iterate until the design is within the ranges proposed in the

Table 1
Geometric parameters of the 3d models.

N	b	$r[mm]$	$a[mm]$	$L[mm]$	$s[mm]$	$t[mm]$	$w[mm]$	n	$E_{beam}[GPa]$	$E_{mass}[GPa]$	$\rho_{beam}\left[\frac{kg}{M^3}\right]$	$\rho_{mass}\left[\frac{kg}{m^3}\right]$	$\varepsilon_{x\,max}[\%]$	m_{ratio}	λ	$\min\frac{\omega_x}{\omega_r}$
1	0.8	20	20	29.5	3.5	0.5	5	10	1	200	1000	7850	3.1	4.6	204	9.2
2	0.85	20	20	7.6	3.7	0.3	6	20	1	200	1000	7850	2.8	29	87	6.8

Supplemental Material (Table S1) to ensure good agreement between 3D and spring-mass resonators. We finally validate the resonator designs of both rotating AMs by comparing resonant frequencies of 3D resonators (calculated using finite elements and Eqs. (4)-(5)) to those of the reduced order model (Fig. 8).

The 3D FEM band structure and transmission results agree well with that of the reduced order model with resonator stiffness according to Eq. (12) (Fig. 9). This shows that (1) stress stiffening effects from rotation can be captured with reduced order models by enforcing a rotation-dependent stiffness of the lumped spring, (2) we can physically realize the required stress stiffening function and attenuate synchronous vibrations in a wide range of frequencies using 3D rotating AM designs.

For the AM that is tuned to first-order synchronous vibrations, the band structure of the 3D model and the reduced order model are almost identical (Fig. 9(ai)). Some slight differences arise at higher rotational speeds where the effects of axial strain on the beam soften the lower edge mode (Fig. 9(ai)). The maximum critical speed and transmission of the 10-unit cell structure also agree well (Fig. 9(aii)). The results show that the designed 3D AM can attenuate first-order synchronous excitations by using rotation to self-adapt the band gap to the synchronous excitation frequency.

The differences between the reduced order and 3D models are more significant in the AM that follows second-order synchronous excitations (Fig. 9(b)). This is because the stress stiffening function differs from Eq. (12) for the larger values of s/L of these resonators resulting in a reduction in maximum critical speed (Fig. 8(b) and 9(bii)). Furthermore, the 3D finite system is less effective at attenuating the synchronous excitation (Fig. 9(bi-bii)). Locally resonant systems have the largest attenuation close to the lower band gap edge (Fig. 7(b-e)). Since the lower band gap edge of the 3D model is lower in frequency compared to the reduced order model (Fig. 9(bi)), the synchronous excitation in the 3D model falls further inside the band gap and thus the attenuation is lower (Fig. 9(bii)).

When physically realizing the system, we expect certain variability among dimensions of the resonators that compose the rotating metamaterial. The variability among resonators breaks the periodicity of the metamaterial adding complexity to the band gap analysis and has been more thoroughly studied in [56,57]. For a given rotational speed, we expect geometric disorder in our system to follow the trends presented in these references. However, the robustness of this rotating metamaterial to geometric disorder increases as rotational speed increases. At the lower rotational speeds, the stiffness of the resonators is dominated by the stiffness of the non-rotating beam (Eq. (16)) and thus it depends on the third order of the beam dimensions. Instead, at higher rotational speeds, i.e. in the asymptotic limits, the stiffness is only inversely proportional to the length of the beam (Eq. (14)). Since the relationship between bending stiffness and beam dimensions is of third order at the low speeds and of first order at the higher speeds the metamaterial becomes more robust to geometric disorder as it approaches the asymptotic limit.

6. Conclusion

In this paper, we study propagating torsional waves in a rotating AM consisting of a shaft with attached linear oscillators that act as local resonances. We showed how the effects of stress stiffening on the local resonances can be modeled by adding a stress stiffening function to the resonator stiffness. We derive the stress stiffening function for a beam-tip-mass resonator and showed that with this stiffening function, the AM can self-adapt its band gaps to attenuate synchronous excitations, typical of rotating machinery, over a wide range of frequencies. We use finite elements to calculate band gaps and transmission of a 3D rotating AM to validate the reduced order model and show that we can physically realize the rotating AM.

This work has applications in attenuating torsional synchronous vibrations in rotating machinery. The stress stiffening effects on AMs can be leveraged to effectively attenuate these synchronous excitations over a wide range of frequencies/ rotational speeds, overcoming the limitations of AMs, which typically have narrow band gaps. Since the band gap depends linearly on the rotational speed, this AM can self-adapt its band gap to the synchronous vibration frequency, which is also linearly dependent on rotational speed. This tuning capability is beneficial since it is completely passive, as there is no need for external controls or sensing for self-adaptation. This AM could be placed in the path of a source of the synchronous excitation (gear, internal combustion engine, compressor) and engineering components to prevent the excitation of synchronous resonances, reducing the number of critical speeds and thus extending the operating range of the machinery.

The beam-tip-mass resonator design studied here can self-adapt their band gaps to and attenuate first- and second-order synchronous vibrations, and the design implementation validates the reduced order models. This specific resonator design does have some limitations. First, it loses its self-adapting capabilities above around 20,000 rpm because the large axial strains (see Supplemental

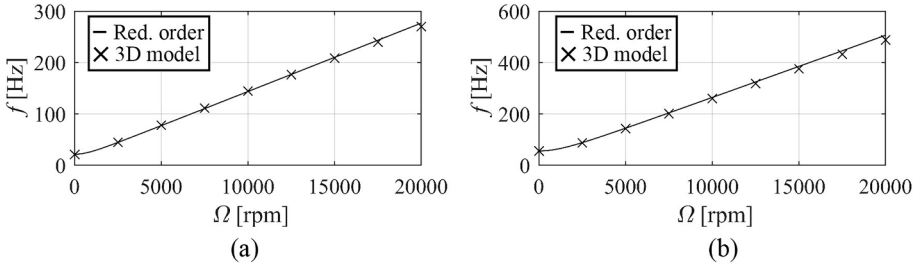

Fig. 8. (a) Resonance frequencies of the beam-tip-mass resonators calculated using the reduced order model and 3D finite element simulations for (a) first synchronous excitations and (b) second synchronous excitations.

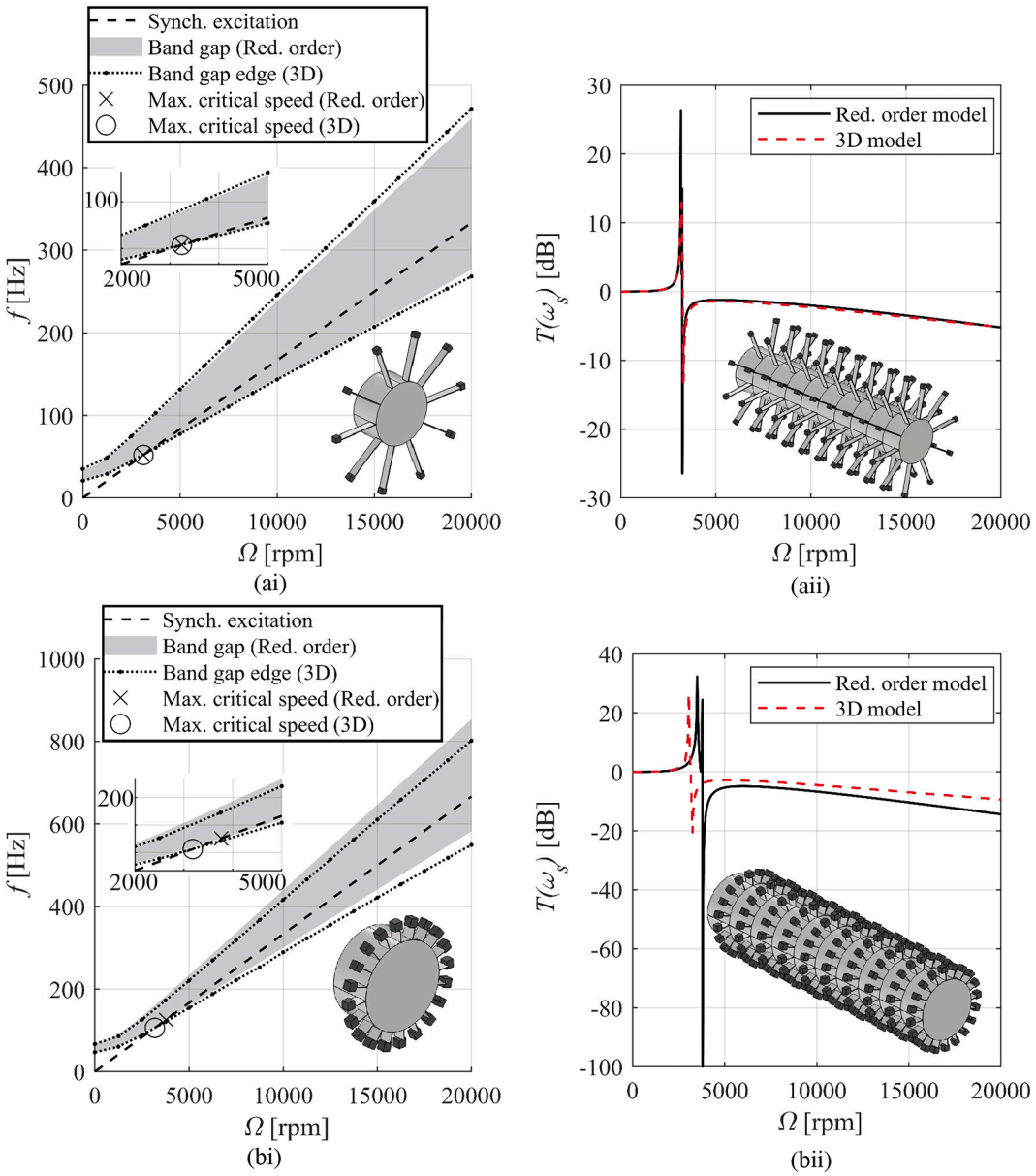

Fig. 9. AMs for attenuation of (a) first-order synchronous excitation and (b) second-order synchronous excitation of plane torsional waves. (i) band gap dependence on rotational speed – insets show band gaps close to the maximum critical speed and 3D AM unit cell, (ii) transmission at the synchronous excitation frequency – insets show the 3D finite AM.

Material) and significant Coriolis forces at high speeds break the linear asymptotic relation between the resonant frequency and rotational speed. Second, higher-order synchronous vibrations above the second order are difficult to target with beam-tip-mass resonances because as the order increases, the required length of the beam decreases (Eq. (15)), thus breaking the Euler-Bernoulli beam assumptions. However, the theory behind the reduced order models presented here is independent of the resonator design and a different physical resonator configuration could overcome these limitations. Overcoming these limitations is significant, as this would enable applications of this concept to high-speed rotating machinery such as turbochargers [58], and to gears with multiple teeth or internal combustion engines with multiple cylinders that are plagued by higher-order synchronous vibrations [34]. The effects of stress stiffening, and more generally those of centrifugal forces, on rotating AMs can be broadened by considering different stress stiffening functions that arise from more complex resonator designs. Studies on rotating beams with distributed mass [8] suggest that blades stiffen as they rotate and can potentially be can leveraged as resonators to attenuate the different synchronous modes in turbines and compressors. Even richer dynamics may be possible by coupling nonlinearity in AMs [59,60] and centrifugal forces. For example, the centrifugal forces could cause nonlinear resonators to vibrate around different equilibrium positions, expanding the range of

possible stress stiffening functions.

This work provides a fundamental understanding of stress stiffening from rotation in AMs. Our results show that the effects of stress stiffening can have a strong influence on the dynamics. This has yet not been studied in the AM community possibly because these effects were negligible for the specific configurations that study rotation in AMs – this suggests that further work would benefit from considering configurations where components of AMs and phononic structures are affected by centrifugal forces. Being able to capture the centrifugal effects results in interesting, unprecedented dynamics such as the ability to control critical speeds and to efficiently attenuate synchronous excitations. This work connects the rotor dynamics community with the phononic crystal and acoustic metamaterial community. This integration is rather unexplored to date, and our work suggests that AMs could introduce novel solutions to rotor dynamics problems.

Declaration of Competing Interest

The authors declare that they have no known competing financial interests or personal relationships that could have appeared to influence the work reported in this paper.

Data availability

Data will be made available on request.

Acknowledgments

This material is based upon work supported by the National Science Foundation under Grant No. CMMI-2031110.

Appendix A. Supplementary data

Supplementary data to this article can be found online at https://doi.org/10.1016/j.ymssp.2023.110689.

References

[1] M.I. Hussein, M.J. Leamy, M. Ruzzene, Dynamics of phononic materials and structures: historical origins, recent progress, and future outlook, Appl. Mech. Rev. 66 (2014), 040802, https://doi.org/10.1115/1.4026911.
[2] Y.-T. Wang, P.-G. Luan, S. Zhang, Coriolis force induced topological order for classical mechanical vibrations, New J. Phys. 17 (7) (2015) 073031.
[3] D. Beli, P.B. Silva, J.R. de F. Arruda,, Mechanical circulator for elastic waves by using the nonreciprocity of flexible rotating rings, Mech. Syst. Sig. Process. 98 (2018) 1077–1096, https://doi.org/10.1016/J.YMSSP.2017.05.022.
[4] P. Wang, L. Lu, K. Bertoldi, H. John, A. Paulson, Topological phononic crystals with one-way elastic edge waves, Phys. Rev. Lett. 115 (2015), 104302, https://doi.org/10.1103/PhysRevLett.115.104302.
[5] L.M. Nash, D. Kleckner, A. Read, V. Vitelli, A.M. Turner, W.T.M. Irvine, Topological mechanics of gyroscopic metamaterials, PNAS 112 (2015) 14495–14500, https://doi.org/10.1073/pnas.1507413112.
[6] Y. Alsaffar, S. Sassi, A. Baz, Band gap characteristics of periodic gyroscopic systems, J. Sound Vib. 435 (2018) 301–322, https://doi.org/10.1016/J.JSV.2018.07.015.
[7] A.A.T. Brandão, A.S. de Paula, A.T. Fabro, Rainbow gyroscopic disk metastructures for broadband vibration attenuation in rotors, J. Sound Vib. 532 (2022), 116982, https://doi.org/10.1016/J.JSV.2022.116982.
[8] R.M. Laurenson, Modal analysis of rotating flexible structures, AIAA J. 14 (1976) 1444–1450, https://doi.org/10.2514/3.61483.
[9] J. Wauer, In-plane vibrations of a thin rotating disk (Deshpande, M., and Mote, C.D., Jr., 2003, ASME J. Vibr. Acoust., 125, No. 1, pp. 68–72), J. Vib. Acoust. 126 (2004) 321–321. https://doi.org/10.1115/1.1691073.
[10] J.C. Simo, L. Vu-Quoc, The role of non-linear theories in transient dynamic analysis of flexible structures, J. Sound Vib. 119 (1987) 487–508, https://doi.org/10.1016/0022-460X(87)90410-X.
[11] V. Ruffini, Coriolis effects in bladed discs, Imperial College of London, 2016.
[12] E. Basta, M. Ghommem, S. Emam, Vibration suppression of nonlinear rotating metamaterial beams, Nonlinear Dyn. 101 (2020) 311–332, https://doi.org/10.1007/s11071-020-05796-z.
[13] K.K. Reichl, D.J. Inman, Lumped mass model of a 1D metastructure for vibration suppression with no additional mass, J. Sound Vib. 403 (2017) 75–89, https://doi.org/10.1016/j.jsv.2017.05.026.
[14] J.D. Hobeck, D.J. Inman, 3D printing of metastructures for passive broadband vibration suppression, in: 20th Int. Conf. Compos. Mater., Copenhagen, Denmark, 2015. https://doi.org/10.13140/RG.2.1.5003.8489.
[15] V. Zega, P.B. Silva, M.G.D. Geers, V.G. Kouznetsova, Experimental proof of emergent subharmonic attenuation zones in a nonlinear locally resonant metamaterial, Sci. Rep. 10 (2020), https://doi.org/10.1038/s41598-020-68894-3.
[16] M. Nouh, O. Aldraihem, A. Baz, Vibration characteristics of metamaterial beams with periodic local resonances, J. Vib. Acoust. 136 (2014), 061012, https://doi.org/10.1115/1.4028453.
[17] M.A. Nouh, O.J. Aldraihem, A. Baz, Periodic metamaterial plates with smart tunable local resonators, J. Intell. Mater. Syst. Struct. 27 (2016) 1829–1845, https://doi.org/10.1177/1045389X15615965.
[18] M.J. Sciiilhansl, R.I. Providence, Bending frequency of a rotating cantilever beam, J. Appl. Mech. 25 (1958) 28–30, https://doi.org/10.1115/1.4011683.
[19] Y.C. Fung, E.E. Sechler, A. Kaplan, On the vibration of thin cylindrical shells under internal pressure, J. Aeronaut. Sci. 24 (1957) 650–660, https://doi.org/10.2514/8.3934.
[20] Z. Liu, X. Zhang, Y. Mao, Y.Y. Zhu, Z. Yang, C.T. Chan, P. Sheng, Locally Resonant Sonic Materials, Science 289 (5485) (2000) 1734–1736.
[21] Y. Xiao, B.R. Mace, J. Wen, X. Wen, Formation and coupling of band gaps in a locally resonant elastic system comprising a string with attached resonators, Phys. Lett. A 375 (2011) 1485–1491, https://doi.org/10.1016/j.physleta.2011.02.044.
[22] C.D. Pierce, C.L. Willey, V.W. Chen, J.O. Hardin, J.D. Berrigan, A.T. Juhl, K.H. Matlack, Adaptive elastic metastructures from magneto-active elastomers, Smart Mater. Struct. 29 (2020) 065004. https://doi.org/10.1088/1361-665X/ab80e4.

[23] C. Nimmagadda, K.H. Matlack, Thermally tunable band gaps in architected metamaterial structures, J. Sound Vib. 439 (2019) 29–42, https://doi.org/10.1016/J.JSV.2018.09.053.
[24] Y. Yao, F. Wu, X. Zhang, Thermal tuning of Lamb wave band structure in a two-dimensional phononic crystal plate, J. Appl. Phys. 110 (2011) 123503. https://doi.org/10.1063/1.3669391.
[25] J.Y. Yeh, Control analysis of the tunable phononic crystal with electrorheological material, Phys. B Condens. Matter 400 (2007) 137–144, https://doi.org/10.1016/J.PHYSB.2007.06.030.
[26] P. Wang, F. Casadei, S. Shan, J.C. Weaver, K. Bertoldi, Harnessing buckling to design tunable locally resonant acoustic metamaterials, Phys. Rev. Lett. 113 (2014), 014301, https://doi.org/10.1103/PhysRevLett.113.014301.
[27] L. Li, A. Cai, Low-frequency band gap mechanism of torsional vibration of lightweight elastic metamaterial shafts, Eur. Phys. J. Appl. Phys. 75 (2016) 10501, https://doi.org/10.1051/epjap/2016160169.
[28] Y. Xiao, J. Wen, X. Wen, Analysis and enhancement of torsional vibration stopbands in a periodic shaft system, J. Phys. D. Appl. Phys. 46 (2013) 145306. https://doi.org/10.1088/0022-3727/46/14/145306.
[29] G. Ma, C. Fu, G. Wang, P. Del Hougne, J. Christensen, Y. Lai, P. Sheng, Polarization bandgaps and fluid-like elasticity in fully solid elastic metamaterials, Nat. Commun. 7 (2016) 13536, https://doi.org/10.1038/ncomms13536.
[30] J. Cabaret, P. Béquin, G. Theocharis, V. Andreev, V.E. Gusev, V. Tournat, Nonlinear hysteretic torsional waves, Phys. Rev. Lett. 115 (2015), 054301, https://doi.org/10.1103/PhysRevLett.115.054301.
[31] I. Arretche, K.H. Matlack, Locally resonant effective phononic crystals for subwavelength vibration control of torsional cylindrical waves, J. Vib. Acoust. 144 (2022) 031007. https://doi.org/10.1115/1.4052748.
[32] I. Arretche, K.H. Matlack, Effective phononic crystals for non-Cartesian elastic wave propagation, Phys. Rev. B 102 (2020), 134308, https://doi.org/10.1103/PhysRevB.102.134308.
[33] T. Feese, C. Hill, Prevention of torsional vibration problems in reciprocating machinery, in: Proc. 38th Turbomach, Symp., Texas A&M University. Turbomachinery Laboratories, 2009, pp. 213–238.
[34] J.C. Wachel, F.R. Szenasi, Analysis of torsional vibrations in rotating machinery, in: Proc. Twenty-Second Turbomach, Symp., Texas A&M University. Turbomachinery Laboratories, 1993, pp. 127–151.
[35] M. Ali, I. Alshalal, J.H. Mohmmed, · J H Mohmmed, Effect of the torsional vibration depending on the number of cylinders in reciprocating engines, Int. J. Dyn. Control. 9 (3) (2021) 901–909.
[36] N. Mizuno, H. Inagaki, T. Nakakubo, M. Nakada, Analysis of synchronous belt vibration in automotive valve train, SAE Tech. Pap. (1988), https://doi.org/10.4271/880077.
[37] T.C.T. Ting, Surface waves in a rotating anisotropic elastic half-space, Wave Motion 40 (2004) 329–346, https://doi.org/10.1016/J.WAVEMOTI.2003.10.005.
[38] M. Schoenberg, D. Censor, Elastic waves in rotating media, Q. Appl. Math. 31 (1) (1973) 115–125.
[39] H. Cetin, G. Yaralioglu, Coriolis Effect on elastic waves propagating in rods, J. Sound Vib. 485 (2020), 115545, https://doi.org/10.1016/J.JSV.2020.115545.
[40] J.G. Simmonds, The in-plane vibrations of a flat spinning disk, Natl. Aeronaut. Sp. Adm. 521 (1962).
[41] M. Deshpande, C.D. Mote, In-plane vibrations of a thin rotating disk, J. Vib. Acoust. 125 (2003) 68–72, https://doi.org/10.1115/1.1522419.
[42] P.W. Likins, F.J. Barbera, V. Baddeley, Mathematical modeling of spinning elastic bodies for modal analysis, AIAA J. 11 (1973) 1251–1258, https://doi.org/10.2514/3.6906.
[43] L. Brillouin, Wave propagation in periodic structures; electric filters and crystal lattices, 1st ed., McGraw-Hill, New York, 1946 https://vufind.carli.illinois.edu/vf-uiu/Record/uiu_1315957/Description (accessed April 11, 2019.
[44] F.B. Pidduck, The vibrations and stability of a rotating cylinder, Proc. Lond. Math. Soc. 2 (1920) 393–402, https://doi.org/10.1112/PLMS/S2-18.1.393.
[45] M. Gürgöze, S. Zeren, The influences of both offset and mass moment of inertia of a tip mass on the dynamics of a centrifugally stiffened visco-elastic beam, Meccanica 46 (2010) 1401–1412, https://doi.org/10.1007/S11012-010-9396-7.
[46] S.V. Hoa, Vibration of a rotating beam with tip mass, J. Sound Vib. 67 (1979) 369–381, https://doi.org/10.1016/0022-460X(79)90542-X.
[47] A.M.S. Budynas, G. Richard, Roark's formulas for stress and strain, ninth edition, 9th ed.,, McGraw-Hill, 2020.
[48] N.C. Perkins, C.D. Mote, Comments on curve veering in eigenvalue problems, J. Sound Vib. 106 (3) (1986) 451–463.
[49] P.A. Deymier, ed., Acoustic metamaterials and phononic crystals, Springe, Berlin, Heidelberg, Berlin, Heidelberg, 2013. https://doi.org/10.1007/978-3-642-31232-8.
[50] D.J. Mead, Wave propagation and natural modes in periodic systems: I. Mono-coupled systems, J. Sound Vib. 40 (1975) 1–18, https://doi.org/10.1016/S0022-460X(75)80227-6.
[51] I. Arretche, K.H. Matlack, Experimental testing of vibration mitigation in 3D-printed architected metastructures, J. Appl. Mech. 86 (2019), https://doi.org/10.1115/1.4044135.
[52] A.A. Boretti, G. Cantore, Comparison of V10 and V12 F1 engines, accessed September 8, 2022, SAE Trans. 107 (1998) 2344–2351, https://www.jstor.org/stable/44736695#metadata_info_tab_contents.
[53] A. Boretti, F1,, turbocharged and downsized ice and kers boost, World J. Model. Simul. 9 (2013) (2014) 150–160.
[54] R. Szczepanik, Analysis of 1st stage compressor rotor blade stress and vibration amplitudes in one-pass jet engine, J. KONES. 20 (4) (2013) 441–450.
[55] M.U. Sohail, H. Elahi, A. Islam, H.R. Hamdani, K. Parvez, R.F. Swati, CFD analysis on the effects of distorted inlet flows with variable RPM on the stability of the transonic micro-compressor, Microsyst. Technol. 27 (2021) 3811–3827, https://doi.org/10.1007/s00542-020-05177-x.
[56] X. An, H. Fan, C. Zhang, Elastic wave and vibration bandgaps in two-dimensional acoustic metamaterials with resonators and disorders, Wave Motion 80 (2018) 69–81, https://doi.org/10.1016/j.wavemoti.2018.04.002.
[57] P. Celli, B. Yousefzadeh, C. Daraio, S. Gonella, Bandgap widening by disorder in rainbow metamaterials, Appl. Phys. Lett. 114 (2019) 091903. https://doi.org/10.1063/1.5081916.
[58] C. Song Gu, Z. Cheng Yuan, Z. Rui Yang, J. Xin Liu, H. Liang Li, Dynamic characteristics of high-speed gasoline engine turbocharger based on thermo-elasto-hydrodynamic lubrication bearing model and flexible multibody dynamics method, Sci. Prog. 103 (2020) 1–23, https://doi.org/10.1177/0036850419897712.
[59] A. Casalotti, S. El-Borgi, W. Lacarbonara, Metamaterial beam with embedded nonlinear vibration absorbers, Int. J. Non Linear Mech. 98 (2018) 32–42, https://doi.org/10.1016/j.ijnonlinmec.2017.10.002.
[60] R.A. Ibrahim, Recent advances in nonlinear passive vibration isolators, J. Sound Vib. 314 (2008) 371–452, https://doi.org/10.1016/J.JSV.2008.01.014.